

RESEARCH ARTICLE | OCTOBER 06 2023

## Vertical electron cyclotron emission diagnostic on the tokamak à configuration variable

A. Tema Biwole ; L. Porte ; S. Coda ; A. Fasoli ; TCV Team



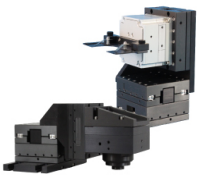
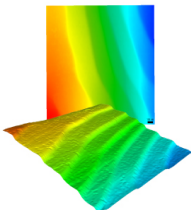
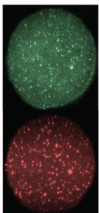


*Rev. Sci. Instrum.* 94, 103504 (2023)

<https://doi.org/10.1063/5.0156000>



CrossMark

 <b>MCL</b> MAD CITY LABS INC. <a href="http://www.madcitylabs.com">www.madcitylabs.com</a>	<p>Nanopositioning Systems</p> 	<p>Modular Motion Control</p> 	<p>AFM and NSOM Instruments</p> 	<p>Single Molecule Microscopes</p> 
---	--	--	---	--

# Vertical electron cyclotron emission diagnostic on the tokamak à configuration variable

Cite as: Rev. Sci. Instrum. 94, 103504 (2023); doi: 10.1063/5.0156000

Submitted: 25 April 2023 • Accepted: 13 September 2023 •

Published Online: 6 October 2023 • Publisher Error Corrected: 10 October 2023



A. Tema Biwole,<sup>a)</sup> L. Porte, S. Coda, A. Fasoli, and TCV Team<sup>b)</sup>

## AFFILIATIONS

Ecole Polytechnique Fédérale de Lausanne (EPFL), Swiss Plasma Center (SPC), CH-1015 Lausanne, Switzerland

<sup>a)</sup>Current address: Massachusetts Institute of Technology (MIT), Cambridge, MA 02139, USA.

Author to whom correspondence should be addressed: biwole@mit.edu

<sup>b)</sup>See authors list in H. Reimerdes *et al.*, Nucl. Fusion 62, 042018 (2022).

## ABSTRACT

In this paper, a diagnostic for the measurement of the electron cyclotron emission (ECE) from non-thermal electrons in magnetically confined fusion plasmas is presented. The diagnostic employs a vertical viewing line of sight that allows us to directly infer the energy of the emitting electrons. Previous incarnations of this diagnostic on other machines have been limited by refraction, which can cause stray radiation to enter the line of sight, polluting the signal. By tuning the toroidal magnetic field on the *Tokamak à Configuration Variable*, TCV, and by carefully selecting the range of frequencies that are used to measure the ECE spectrum, refraction can be mitigated and background radiation power reduced to below the noise power of the instrumentation. A novel technique for calibrating the diagnostic based on plasma measurements and modeling has been developed. The paper will describe the Vertical ECE (V-ECE) diagnostic on TCV, the calibration method, and the first results from the measurements.

© 2023 Author(s). All article content, except where otherwise noted, is licensed under a Creative Commons Attribution (CC BY) license (<http://creativecommons.org/licenses/by/4.0/>). <https://doi.org/10.1063/5.0156000>

## I. INTRODUCTION

In the quest for fusion energy, the so-called non-thermal electrons have fascinated scientists, ever since they were noticed. They trigger serious concerns in tokamaks, as they can be accelerated in an uncontrolled way via the “run-away” phenomenon. They are also of interest for the role they play in the sustainment of plasma current using radio frequency (RF) waves. In both cases, it is important to be able to measure their energy distribution. The ECE (Electron Cyclotron Emission)<sup>1</sup> spectrum has been considered for many decades now as a serious candidate for the diagnosis of electron energy distribution. It is very well established in the literature how to obtain the ECE spectrum from the electron distribution.<sup>2,3</sup> Complex is to solve the inverse problem, that of obtaining the distribution from the ECE spectrum. The complexity arises from the spectrum itself, which is determined both by the density of (non-thermal) electrons in phase space and the gradient of the magnetic field along the ECE line of sight. Electrons at different energies with different velocity components with respect to the magnetic field, located at different locations along the line of sight, can satisfy the resonance condition and contribute to the ECE radiation. In

addition, the ECE total radiation is not straightforwardly the sum of the single emissions. In fact, each emitting electron can absorb the radiation emitted by another electron in its neighborhood. It is the complicated convolution of the physical and energy spaces contained in the ECE spectrum that makes it difficult to invert. Good quantitative results were found on TCV, the *Tokamak à Configuration Variable*, 20 years ago with a horizontal line of sight<sup>4</sup> measuring from the High Field Side (HFS ECE) (see Fig. 1). The results revealed the presence of electrons up to 45 keV of energy (ten times the bulk energy). Precise inversion of the spectrum was, however, difficult to achieve due to the uncertainty about the location of the emitting electrons. Such a limitation also applies to a horizontal line of sight with measurement from the Low Field Side (LFS ECE).<sup>5</sup> Efforts to ease the inversion are made by constraining the regions in the physical and energy spaces that contribute to the radiation. This has been achieved in this work using a configuration that views along a constant magnetic field region in the plasma, a Vertical ECE (V-ECE). The V-ECE, by viewing the plasma perpendicular to the magnetic field gradient, can, in principle, guarantee a one-to-one correspondence between energy and measured frequency (see Fig. 1). The proviso is to minimize the harmonic

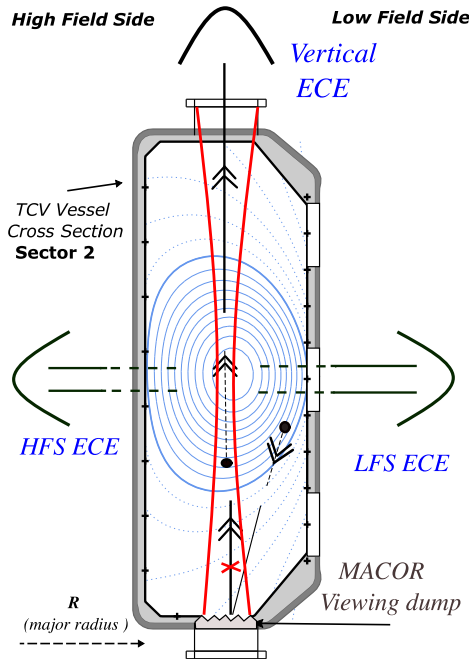


**FIG. 1.** Cross-sectional view of the TCV vessel showing the V-ECE line of sight, along with more traditional ECE views from the Low Field Side and High Field Side directions (LFS ECE and HFS ECE). The V-ECE line of sight terminates on a MACOR viewing dump, which prevents measurement of stray radiation.

overlap and multiple wall reflections. At high harmonics, the overlap is extreme making the spectrum almost a continuum. At lower harmonics, the discrete nature of the harmonics remains (see Fig. 2 for an illustration of harmonic overlap). V-ECE measurements at lower harmonics have been attempted in the 1980s and 1990s on Alcator,<sup>6</sup> PLT<sup>7</sup> and TORE SUPRA.<sup>8–10</sup> The control of plasma refraction and multiple wall reflections then emerged as a major issue for V-ECE. In the early 1990s, an attempt was made on DIII-D,<sup>11</sup> where plasma refraction constrained the use of harmonics above the fifth. The attempt thus had to deal with the problem of high harmonic overlap. More recently, multiple wall reflections were a show-stopper on COMPASS during another V-ECE attempt in the absence of a viewing dump.<sup>12</sup> In the absence of a viewing dump on COMPASS, good interpretation of the data was made almost impossible by the high level of contamination in the measured signals. The V-ECE of TCV, which is equipped with a viewing dump,<sup>13</sup> was simulated using the ray-tracing code SPECE<sup>14</sup> to identify its optimal operating conditions. The system is calibrated using the plasma itself and can measure simultaneously polarized ECE waves from the second to the fourth harmonic. In Secs. II A–IV A, we recall the principle of V-ECE measurements, describe the diagnostic system, and present the calibration idea. Some of the experimental measurements achieved with the diagnostic will be presented in Sec. V.

## II. DESCRIPTION OF THE DIAGNOSTIC SYSTEM

### A. Measurement principle

The radiation frequency,  $\omega$ , obtained from the ECE perpendicular resonance condition can be expressed as

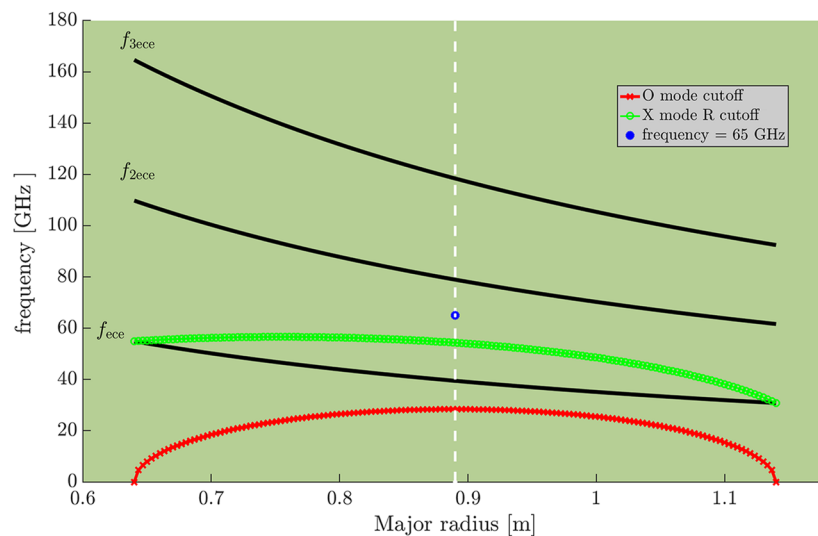


**FIG. 2.** Electron cyclotron resonances, O-mode cutoff and X-mode right cutoff simulated in a TCV plasma with a central magnetic field of  $\sim 1.41$  T and a peak electron density of  $\sim 1 \times 10^{19} \text{ m}^{-3}$ . The V-ECE radius of measurement is illustrated with the white dashed line. For a V-ECE measurement in these conditions, the frequencies should be chosen to be higher than the cutoff frequencies. The chosen frequencies should also lie below the electron cyclotron frequencies in order to measure downshifted cyclotron radiation from non-thermal electrons. The issue of harmonic overlap occurs when, for example, at a frequency of 65 GHz (blue dot), the instrument measures downshifted radiation from both the second and third harmonics of the cyclotron frequency:  $f_{2ece}, f_{3ece} = 2, 3 \times f_{ece}$ . The ratio of cyclotron frequencies between consecutive harmonics decreases with increasing harmonic numbers, worsening the harmonic overlap at higher harmonics.

$$\omega = \frac{n\omega_{ece}}{\gamma}, \quad (1)$$

where  $n$  is the harmonic number,  $\gamma$  is the relativistic factor, and  $\omega_{ece}$  is the fundamental electron cyclotron emission frequency. In a tokamak geometry, where  $R$  is a measure of the major radius, Eq. (1) can be rewritten as

$$\omega \propto \frac{n|e_{ch}|B_0R_0}{\gamma m_{e0}R} \propto \frac{n}{\gamma R}. \quad (2)$$

Here,  $R_0 = 0.88$  m is the tokamak major radius, and  $B_0$  is the central magnetic field. The constants  $e_{ch}$  and  $m_{e0}$  are, respectively, the electron charge and the electron rest-mass. The proportionality in Eq. (2) suggests that in the case of an ideal vertical line of sight (fixed major radius  $R$ ), with emission arising from a single harmonic  $n$ , the radiation frequency is solely a function of the energy of the emitting electrons,  $\omega \propto \frac{1}{\gamma}$ . From the measured frequency,  $f = \omega/2\pi$ , the kinetic energy of the emitting electrons can be calculated as

$$E = m_{e0}c^2 \left( \frac{nf_{ece}}{f} - 1 \right), \quad (3)$$

with  $f_{ece} = \omega_{ece}/2\pi$ ,  $c$  being the velocity of light. From Eq. (3), it can be seen how, in ideal V-ECE conditions, any broadening in the measured frequency is due to the presence of electrons at different energies. This one-to-one correspondence between energy and measured frequency is the fundamental principle behind electron distribution measurements with V-ECE. The finite beam size of the optical arrangement and the finite bandwidth around each measured frequency cause a spread on the measured frequency and are responsible for the finite resolution in the energy of the system.

## B. Radiometry: Frequencies and harmonics

The V-ECE diagnostic on TCV uses a set of heterodyne radiometers. The radiometers cover the frequency ranges 78–114, 125–130, and 133–148 GHz, as can be seen in Fig. 3. Figure 4 shows a block diagram of the detection system including one of the radiometers, starting from the transmission line up to the acquisition. The radiation from the plasma, typically in the frequency range 30–200 GHz, travels in the transmission line to reach the microwave components of the detection system. The microwave components include a set of notch filters in the front face to protect the system against the Electron Cyclotron Heating (ECH) power, which

may reflect off the vessel to reach the transmission line. The notch filters are centered at the gyrotron X2 and X3 frequencies (~82 and ~118 GHz) with power attenuation up to 70 dB. A variable power attenuator is used in series to fine-tune the intensity of the incoming power. This is of practical importance since the ECE intensity depends on the plasma scenario and can vary by orders of magnitude (up to  $\sim 10^2$ ) in the presence of non-thermal electrons. A 3 dB directional coupler splits the filtered RF power into the different branches of the heterodyne receiver. The heterodyne receiver then processes the radiation up to the acquisition in three main stages: the RF stage, the Intermediate Frequency (IF) stage, and the video stage. The RF stage is where the frequency of the incoming radiation is shifted to a lower frequency for further processing. The need to downshift the incoming RF frequency has historically been motivated by technological constraints in the fabrication of microwave components. In the RF stage, the frequency conversion happens in the mixer, a diode with a non-linear  $I/V$  characteristic.

High Pass Filters (HPFs) are used before the mixing elements to ensure that only the frequencies above each LO frequency can reach the mixer. A frequency isolator in the higher frequency circuit is used to avoid, in the low frequency circuit, the detection of some frequencies coming from the LO in the high frequency circuit. The IF stage, after the mixing elements, is identical for both circuits. In the IF stage, the signals are amplified, fed into a power divider, and split into 12 frequency bands with the help of bandpass filters (BPFs), each ~750 MHz wide. Each frequency band constitutes a channel whose RF frequency band is determined by the IF filter bandwidth. The filtered signals are rectified in the diode detector and further processed in the video stage. In the so-called video stage, the signals are amplified and low-pass filtered down to 100 kHz for the acquisition.

## C. Optics

The optical arrangement of the V-ECE antenna is designed to produce a line of sight in the tokamak with minimal radial extent. The V-ECE antenna design is based on Gaussian beam optics.<sup>15</sup> The antenna exploits a top port of 20 cm in diameter, centered at the major radius  $R = 88$  cm, on top of which an ellipsoidal mirror of a focal length of ~61 cm is fastened. The aperture of the top port is 163.4 cm from the machine floor, and the center of the mirror is ~101 cm above the vessel mid-plane. The height of the beam waist is desired near the vessel mid-plane at  $Z \approx 20$  cm. The mirror is made out of copper, while the vacuum window at the port is made of

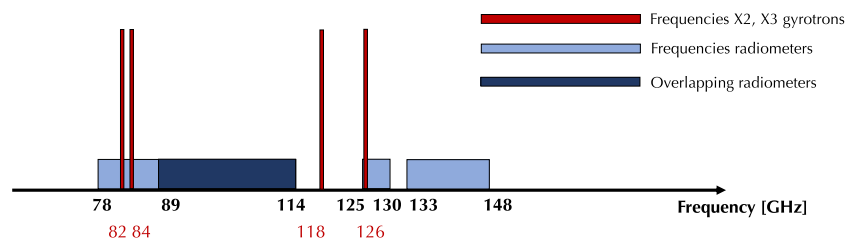


FIG. 3. Frequency coverage of the V-ECE on TCV, showing the overlapping frequencies and the gyrotrons X2 and X3 frequencies.



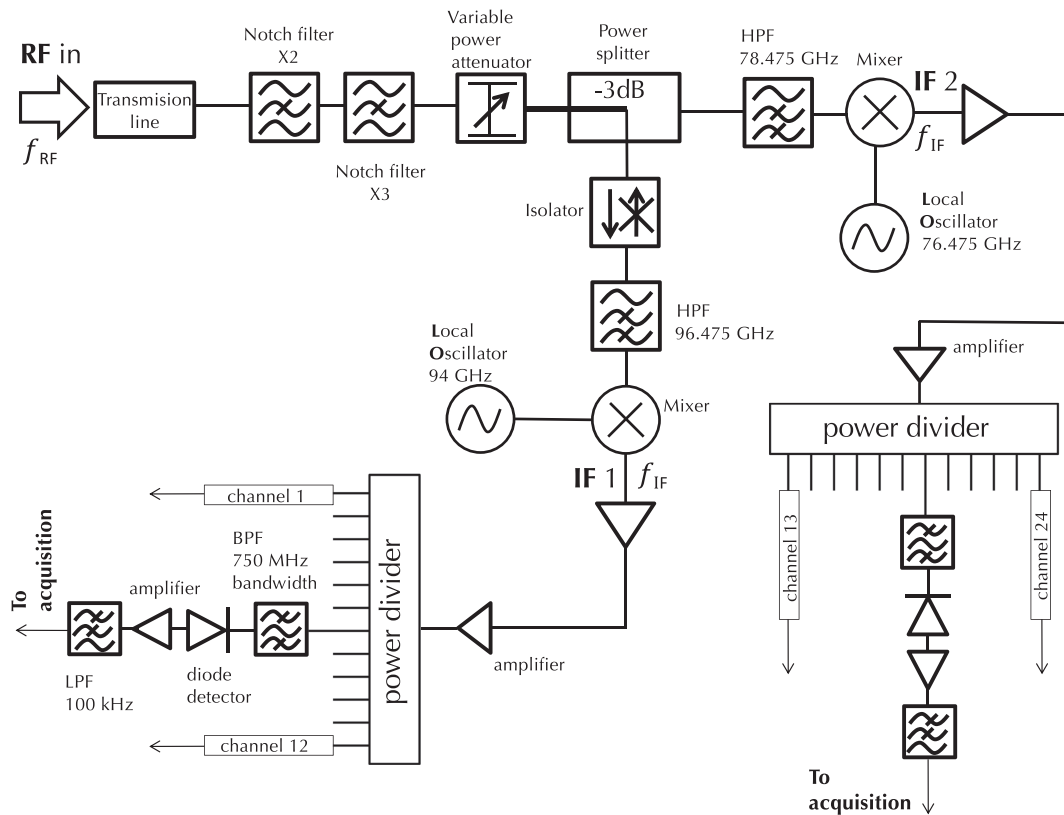


FIG. 4. An overview of the detection system for the V-ECE on TCV, illustrating the radiation path from the transmission line to the acquisition.

alumina and is thus opaque to visible light. The design of the mirror is refined by optimizing the size of the beam in the toroidal direction to have equal beam sizes in the radial and toroidal directions. The antenna, by design, favors the free propagation of the electromagnetic radiation, or the propagation in low loss waveguides to limit the attenuation of the radiation. The radiation from the plasma, after the focusing mirror, is collected in an oversized corrugated waveguide of 63.5 mm in diameter. The waveguide aperture is positioned  $\sim 72$  cm from the mirror center to transport the plasma radiation to a quasi-optical telescope manufactured by *Thomas Keating Ltd.* in the United Kingdom. The quasi-optical telescope is optimized for frequencies in the W band. It is equipped with a wire grid polarizer, broadband scalar horns, and focusing mirrors. The wire grid polarizer separates the incoming beam into two polarizations, each of which is collected in a horn and fed into the transmission lines for detection. Alignments of the system are achieved during machine vents by means of visible light from a diode laser. The diode laser is usually connected to one of the horns, and the light position is measured at the bottom of the machine. The stability of the alignment can be of concern due to the mechanical vibrations of the vessel. However, misalignments of the line of sight are identified by exploiting the value of the resonant magnetic field at the measuring frequencies. That is misalignments generally should not significantly affect the studies using the diagnostic. A drawing of the V-ECE antenna on TCV Fig. 5.

### 1. The beam size

The effective size of the antenna beam is an important parameter for diagnostics, since it influences the energy resolution and the conditions for non-thermal emission measurements. We show in this paragraph the estimates of the beam size effectively produced by the antenna. The size of the beam is defined by the extent of the  $1/e^2$  intensity level in the assumed Gaussian beam. The designed beam waist is 3 cm in radius and is located  $\sim 20$  cm above the vessel mid-plane, i.e., 81 cm away from the mirror and 95 cm from the machine

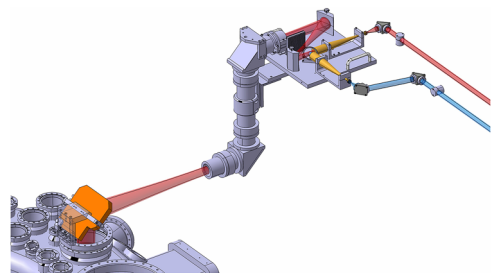
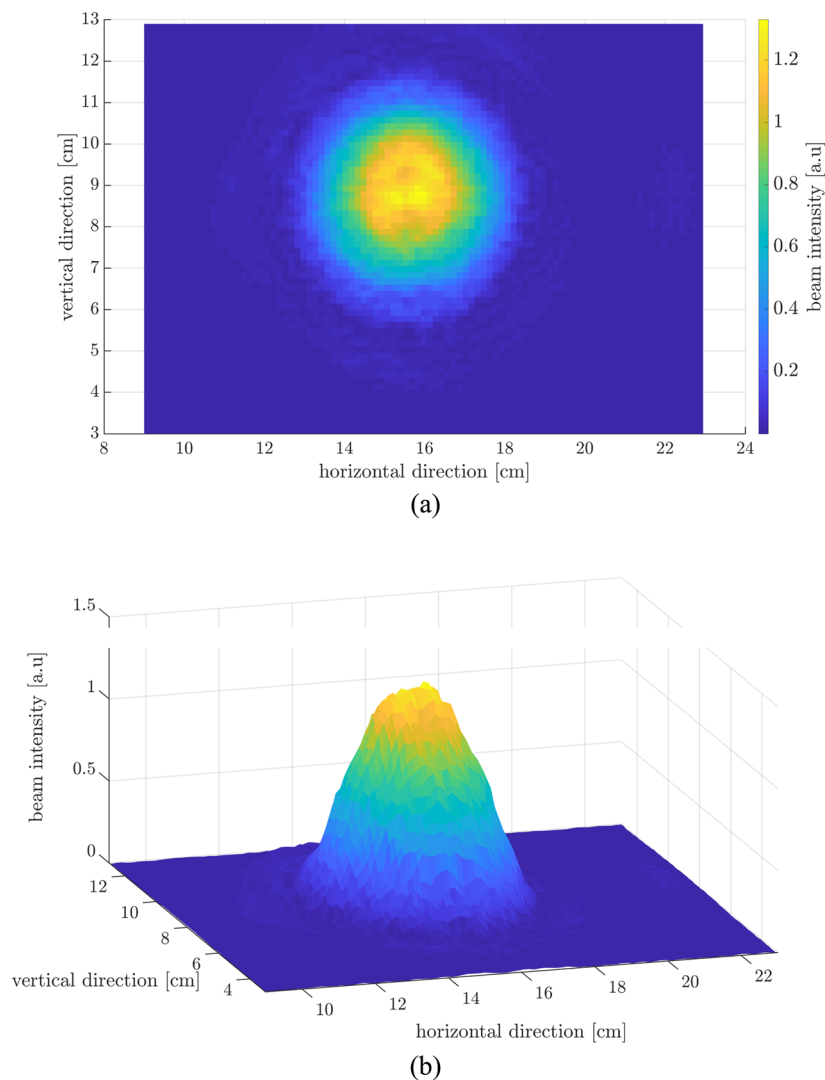


FIG. 5. Layout of the V-ECE antenna beam pattern out of the vessel. The radiation from the plasma is focused by the ellipsoidal (copper) mirror and transported to the quasi-optical telescope by the corrugated waveguide.

floor. The size of the beam is 4 cm on the mirror and 5 cm on the floor. According to the design, the mirror produces a beam waist of 4 cm at the position of the waveguide at 72 cm from the mirror in the direction toward the detection system. The beam divergence in a vacuum is calculated to be  $\approx \arctan \frac{10^{-6}}{2 \times 95} = 2.14^\circ$ . The designed beam is thus well collimated along the 176 cm path from the mirror to the machine floor.

For the measurement of the beam size, an ensemble comprised of the quasi-optical telescope, the HE11 waveguide, and the rotated ellipsoidal mirror was used to produce the beam along a horizontal direction in the air outside the vacuum vessel. That is performed for practical reasons, assuming that the size of the beam is not affected by the mirror rotation. The horizontal and vertical axes of the beam in this setup are equivalent, respectively, to the radial and toroidal axes of the beam produced in the vessel. A transceiver module of a

Portable Network Analyser was connected to a horn on the quasi-optical telescope, irradiating the system with 6 dBm of power at a frequency of  $\sim 100$  GHz. A receiver module was used to measure the amplitude of the electric field of the beam. A WR08 rectangular waveguide was attached to the receiver's test port to allow the module to be recessed and screened with an absorber, improving the quality of the measurement. A robot scanning the vertical and horizontal directions with fine steps ( $<1$  mm) was used to allow the receiver module to scan the beam area. As a test, the beam size was measured before the reflection of the mirror at the aperture of the HE11 waveguide. The results are shown in Fig. 6. The measurement suggests a beam of the same size,  $\sim 2.8$  cm, in both horizontal and vertical directions. A measurement of the size of the beam reflected off the mirror was attempted. The receiver module was positioned  $\sim 50$  cm from the mirror center. The beam size at



**FIG. 6.** Result of the beam size measurement at the aperture of the HE11 waveguide. The beam intensity is shown in the upper view (6a) and in elevation view (6b).

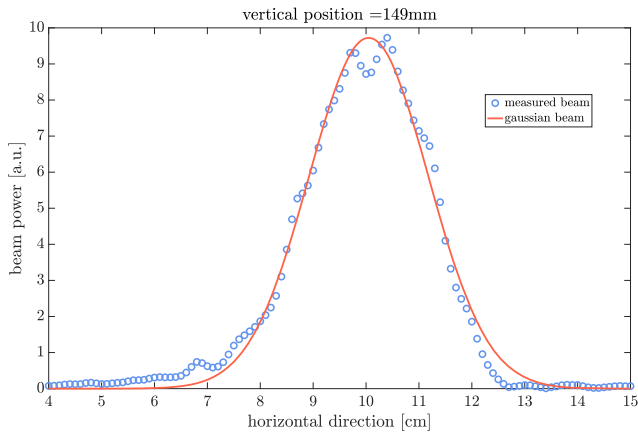


FIG. 7. Measured beam size compared to a Gaussian beam.

this location would correspond to the size of the beam at  $\sim 50$  above the vessel mid-plane. The measured beam shown in Fig. 7 suggests a Gaussian beam of  $\sim 2.3$  cm with a frequency of 100 GHz. In the same figure, a superposition of a theoretical Gaussian beam of the same size suggests that the beam produced by the antenna can be assumed to be Gaussian at  $\sim 50$  cm from the mirror. It can be concluded that in vacuum, the radial extent of the antenna beam at 100 GHz is  $\sim 2.3$  cm at  $\sim 30$  cm above the waist position. The toroidal extent of the beam is considered to be approximately equal to its radial size. The measured beam sizes are thus consistent with the designed beam.

Another approach, using experimental plasma discharges to infer approximately the magnitude of the beam size, is also presented. The idea is as follows: during a plasma discharge, the magnetic field is ramped up or down such that the resonance of one of the harmonics of the fundamental cyclotron frequency crosses the antenna line of sight. When the resonant frequency within the

line of sight corresponds to the frequency of the radiometers, the time trace on that frequency channel during the field ramp carries information on the beam size. That is, the time the resonance spends within the line of sight is mainly due to the radial extent of the antenna beam pattern. It is possible in our case to infer the size of the beam from the time trace on each channel only because the size of the antenna pattern is supposedly much larger than the size of the resonant emission layer. If the size of the emission layer was larger than the beam size, the signal time trace would carry information on the width of the emission layer instead. A set of plasma discharges with magnetic field ramps has been considered. The time interval during which the resonance crosses each channel is used to infer the corresponding change in the magnetic field (see Fig. 8). Using the change in magnetic field,  $\Delta_B$ , the radial extent of the beam pattern,  $\Delta_R$ , is readily obtained via the equivalence

$$\Delta_R = \frac{nR_0|e_{ch}|}{2\pi m_{e0}f} \Delta_B. \quad (4)$$

The time interval in the signal trace around the peak was limited to the extent of the  $1/e^2$  intensity level to ensure that the reconstructed beam size is within the  $1/e^2$  intensity level. Note that the beam size that is inferred is the size of an antenna pattern undergoing interaction with the plasma (not the size in a vacuum). Consequently, the average size deduced by this method represents the upper limit of the antenna beam size in vacuum.

The result obtained for a few plasma discharges at frequencies close to 100 GHz suggests an average size of the beam diameter close to  $\sim 6$  cm. The larger beam size in the plasma compared to the measurements in air is due, among others, to the refraction of the beam in the plasma. Concerning the location along the vertical axis of the beam, this approach cannot provide an accurate answer. The inferred size is certainly the beam size within the plasma. The exact plasma height to which this size is associated depends on the optical depth of the plasma. The optical depth of the detected X3 resonance

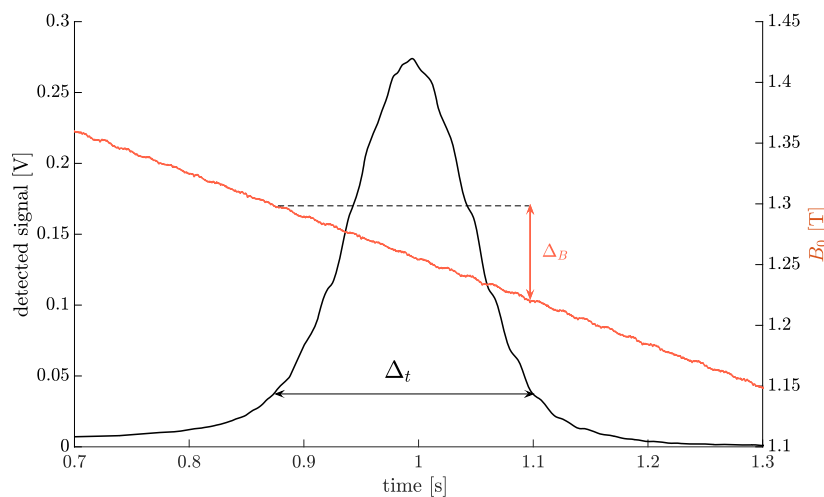
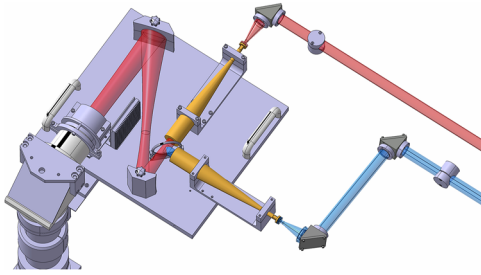


FIG. 8. Response of a channel of the detection system to a magnetic field ramp. The time interval delimits the drop by  $1/e^2$  in the signal intensity.



**FIG. 9.** Splitting of the V-ECE beam into X- and O-modes at the wire grid polarizer installed on the quasi-optical telescope.

scales with the electron temperature like  $\sim T_e^3$  (see Ref. 1 for derivation). Therefore, there are good reasons to believe that the inferred beam size can be the beam size near the center of the plasma. For these experiments, the plasma center was at  $Z = 0$  cm,  $\sim 20$  cm below the waist height.

## 2. The wave polarization

The V-ECE on TCV is designed to measure, for each frequency, the extraordinary (X-) and ordinary (O-) polarizations of the radiation. The wave polarization is calculated for a cold plasma in the Appleton-Hartree/Stix framework (see Sec. IV of Ref. 16 for the expressions of the indices of refraction). For perpendicular, upward propagation  $\vec{k} \perp \vec{B}$  ( $\vec{k}$  being the wave vector and  $\vec{B}$  the local magnetic field), the electric field of the O-mode wave oscillates along the local magnetic field. The electric field of the X-mode describes an elliptic orbit in the plane perpendicular to the local magnetic field. Given that the propagation is perpendicular to the magnetic field, the X-mode has both longitudinal and transverse components.

The orientation of the electric field that is considered in the measurements is at the last closed flux surface. The electric field of the O-mode is aligned with  $\vec{B}$ , and that of the X-mode is perpendicular to  $\vec{B}$  and  $\vec{k}$ . In a hypothetical case of a magnetic field with just the toroidal component, the electric field of the O-mode would be aligned in the toroidal direction and that of the X-mode in the radial direction. In that case, the polarizations at the wire grid in the quasi-optical telescope (Fig. 9) would be vertical and horizontal for the X- and O-modes, respectively, assuming the polarization had not changed during the reflections on the antenna components. The wire grid reflects the polarization that has its electric field parallel to its fibers and lets through the polarization with an electric field perpendicular. For V-ECE experiments, the precise direction of the magnetic field vector is calculated, accounting for the poloidal and toroidal components. The direction of the electric field vectors for the O- and X-modes is inferred, propagated through the mirror using ECPOL,<sup>17</sup> and separated at the wire grid. The poloidal component of the magnetic field shifts the ideal polarizations (vertical and horizontal) by a few degrees typically. It is very important to avoid cross polarization on the grid by fixing a precise angle. This is because the ratio in a typical thermal plasma of the X- to O-mode intensities is of the order of  $10^2$  (see work from Bornatici in Ref. 1), and the single particle calculation in Ref. 16 provides more detail on relative X- to O-mode intensities. A scrambling of the X- to the O- mode of just 1% would completely shadow the original O-mode emission from the plasma.

## D. Energies and resolution

### 1. Energies

For the calculation of the energies measured by the system, we assume that the detected radiation is a direct emission originating

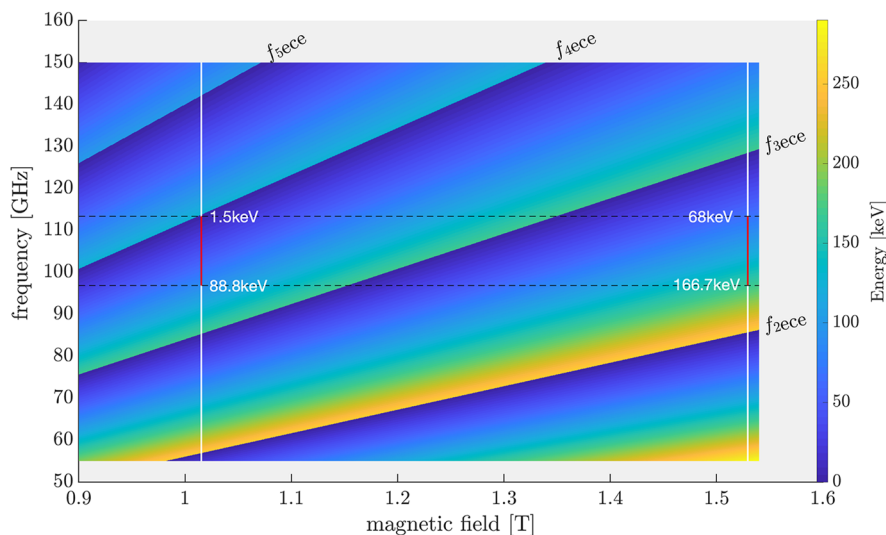


**FIG. 10.** Energy map of the V-ECE on TCV. The map shows the V-ECE energy as a function of frequency and (central) magnetic field. The oblique lines are the fundamental ECE frequencies for a few harmonics. The V-ECE energy ranges in the 96–114 GHz frequency range for two values of magnetic field  $\sim 1.01$  and  $\sim 1.53$  T are shown using the vertical red lines. The figure illustrates the dependence of the measured energy at a given frequency on the central magnetic field value.

within the diagnostic line of sight with minimized harmonic overlap. With those assumptions, Eq. (3) can be used to calculate the kinetic energy of the electrons whose emission is detected. Figure 10 shows the result of the calculated energies in a map where the values of energies at the field value of 1.4 are highlighted.

The measurements at the available frequencies can, in theory, span from the downshifted second harmonic ( $f_{2ece}$ ) to the downshifted sixth harmonic ( $f_{6ece}$ ). The energy measured by a frequency is determined by the frequency difference between that frequency and the frequency of the upward harmonic of the fundamental cyclotron frequency. That distance depends only on the value of the magnetic field. Changing the value of the field allows each frequency to probe a different region of the phase space. This situation is equivalent, in physical space, to the antenna, which is fixed vertically, and and the cold resonance of the harmonic of the measured frequency that is shifted in the radial direction by a change in the magnetic field. The diagnostic can only measure downshifted emission from the harmonics at the lower field side of the line of sight. At a given frequency, the energy measured will be higher if the line of sight is far from the cold resonance of the harmonic. Like-wise, lower energies are measured if the line of sight is closer to the cold resonance of the harmonic, where the bulk electrons of the emission layer emit. The system can then measure energies up to  $\sim 250$  keV without harmonic overlap at  $\sim 80$  GHz from radiation emitted at the downshifted third harmonic, as illustrated in Fig. 10.

## 2. Resolution

We recall Eq. (1): the relativistic factor  $\gamma$  of a resonant electron in the absence of harmonic overlap is proportional to

$$\gamma \propto \frac{B}{f}. \quad (5)$$

The energy resolution (broadening of  $\gamma$ ) is determined by the broadening in both the magnetic field and the measured frequency. The Gaussian beam diameter, which is  $\sim 6$  cm wide in the plasma center, introduces a broadening  $\frac{\delta\gamma}{\gamma}|_{\text{beam}}$  in the order of 7%. The radial aperture of the antenna causes a broadening of the magnetic field; the toroidal aperture of the same size leads to a frequency uncertainty due to the Doppler effect. The uncertainty due to the Doppler shift,  $\frac{\delta\gamma}{\gamma}|_{\text{doppler}}$ , is calculated to be less than 4%. The radiometer introduces frequency broadening due to the 750 MHz bandwidth around each measured frequency. The corresponding broadening,  $\frac{\delta\gamma}{\gamma}|_{\text{instrument}}$ , is evaluated to be less than 1%. The poloidal magnetic field, which is not constant along the vertical direction in the vessel, introduces a broadening of at most  $\frac{\delta\gamma}{\gamma}|_{\text{poloidal}} = \frac{\delta B}{B} \sim 1\%$ . The maximum total uncertainty

$$\frac{\delta\gamma}{\gamma} = \frac{\delta\gamma}{\gamma}|_{\text{beam}} + \frac{\delta\gamma}{\gamma}|_{\text{doppler}} + \frac{\delta\gamma}{\gamma}|_{\text{instrument}} + \frac{\delta\gamma}{\gamma}|_{\text{poloidal}} \simeq 13\%. \quad (6)$$

This resolution in the relativistic factor is calculated for the worst cases and is not constant across the whole frequency range. In fact, the antenna beam pattern depends on the frequency and is narrower at high frequencies. We expect up to 5% lower resolution for the higher frequencies, also because the instrumental broadening decreases further with frequency. We use an average  $\frac{\delta\gamma}{\gamma} = 10\%$  to illustrate the effect on the energy resolution of the broadening of the relativistic factor. The energy resolution  $\frac{\delta E}{E}$  can be expressed in terms of  $\frac{\delta\gamma}{\gamma}$  by manipulating the expression of the relativistic kinetic energy,  $E = (\gamma - 1)m_{e0}c^2$ , as

$$\frac{\delta E}{E} = \frac{\delta\gamma}{\gamma} \left( 1 + \frac{m_{e0}c^2}{E} \right). \quad (7)$$

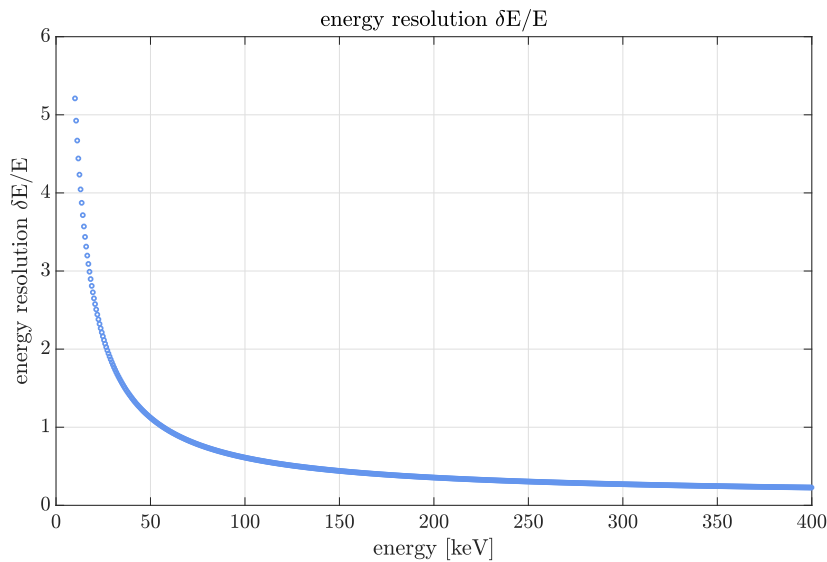


FIG. 11. Energy resolution  $\frac{\delta E}{E}$  of the V-ECE diagnostic expressed as a fraction (for convenience) and calculated with a constant value of  $\frac{\delta\gamma}{\gamma} = 10\%$ .



Equation (7) shows that the energy resolution, in the first order, decreases for higher energy (see Fig. 11). An estimation of  $\frac{\delta\gamma}{\gamma}$  for each frequency should, however, be performed for a rigorous estimation of the energy resolution. Improvements in the energy resolution are possible via the factor  $\frac{\delta\gamma}{\gamma}$ , which depends on the frequency and is directly proportional to  $\frac{\delta E}{E}$ . A solution is to use the higher frequencies to measure the lower energies where the resolution needs to be improved.

### III. CONDITIONS FOR V-ECE MEASUREMENTS ON TCV

Some conditions, in terms of plasma parameters, are required for V-ECE measurements. The conditions are required such that the detected radiation originates within an isolated vertical volume in the tokamak. By design, the antenna pattern is vertical and terminates on the viewing dump (see Fig. 1). Multiple reflected rays, to reach the antenna line of sight, should first reach the highly absorbing viewing dump. However, during plasma discharges, the refraction in the plasma shifts the antenna pattern, which may now miss the viewing dump. The plasma conditions that are required are those that minimize the refraction of the antenna beam in the plasma, allowing the V-ECE line of sight to fall within the viewing dump. In this section, we also brief on the conditions needed to avoid the cutoff of the waves, shown in Fig. 2.

#### A. Density cutoff

Calculations using the cold plasma dispersion relation yield the density values required to avoid the wave cutoff. In general, the cutoff density for the O-mode depends solely on the wave frequency, while the cutoff density for the X-mode also decreases with the magnetic field. The cutoff densities for the X-mode have been computed at the highest possible value of the magnetic field within the V-ECE line of sight,  $\sim 1.54$  T, to obtain the lowest densities in the plasma needed for the X-mode cutoff. An electron density of at least  $\sim 7.94 \times 10^{19} \text{ m}^{-3}$  in O-mode and  $\sim 3.67 \times 10^{19} \text{ m}^{-3}$  in X-mode are needed to have a wave at 80 GHz in cutoff. The density limit is lower in the extraordinary mode yet still higher than the typical densities that can be used for V-ECE measurements. We note that most of the V-ECE experiments will use the X2 gyrotrons to create non-thermal electrons and that the X2 gyrotrons operate at a frequency close to 80 GHz. That means we would anyway be constrained in those experiments to stay below the cutoff density limit for X mode to ensure that the gyrotron wave itself does not enter the cutoff. Many of the other plasma experiments for V-ECE require lower densities. We consider, in general, that the wave cutoff of both polarizations is avoided during V-ECE measurements.

#### B. Plasma refraction and multiple wall reflections

The antenna beam pattern is simulated using the ray tracing code SPECE.<sup>14,18</sup> We attempt to find a window of electron density that certainly minimizes the effect of the beam refraction in the plasma. Minimizing the refraction means finding a window of plasma parameters that allows the antenna beam intensity to mainly fall within the viewing dump after its interaction with the plasma. As

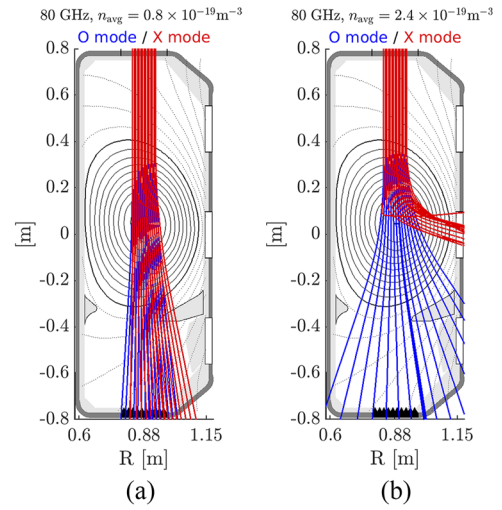


FIG. 12. Simulation of rays' trajectories for a wave at 80 GHz with scan of the line averaged density from  $0.8 \times 10^{-19} \text{ m}^{-3}$  (12a) to  $2.4 \times 10^{-19} \text{ m}^{-3}$  (12b).

input, the simulation requires a plasma equilibrium, an electron density, and temperature as a function of  $\psi$ , the normalized toroidal flux. Figure 12 shows the results of the modeling for a wave at 80 GHz in the O-mode and X-mode for different electron densities, and Fig. 13 for a wave at 150 GHz. The simulations are performed with the same plasma equilibrium. The input electron density at each  $\psi$  is multiplied by the same factor to obtain the different values of line averaged density and to isolate the only effect of the density on the refraction. There is no need to modify the input temperature as it has no effect on the beam refraction.

The general considerations from Figs. 12 and 13 are as expected from the cold plasma theory: the refraction effect is worst at the

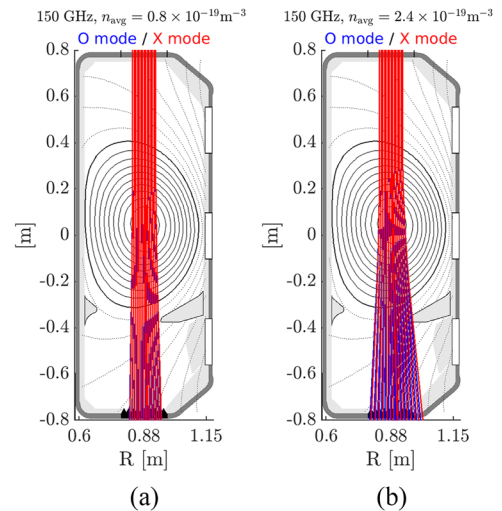


FIG. 13. Simulation of rays' trajectories for a wave at 150 GHz with scan of the line averaged density from  $0.8 \times 10^{-19} \text{ m}^{-3}$  (13a) to  $2.4 \times 10^{-19} \text{ m}^{-3}$  (13b).



lower frequencies and at the higher densities. The dependence of the beam refraction on the frequency can be understood from the expressions of the indices of refraction derived within the cold plasma approximation. The refractive indices for both polarizations, in general, increase asymptotically with frequency. The refraction effect is worst for the X-mode since its index of refraction is always lower than that of the O-mode. In the simulation of the wave at 80 GHz, the most explicit effect is that of the density on the beam refraction. The density gradient drives the change in the refractive index and thus induces beam refraction. By multiplying the densities at each  $\Psi$  by a constant factor and keeping the magnetic equilibrium frozen, the density gradient was also increased. The consequence is the increased effect of refraction on the beam at higher densities. Figure 12(b) shows the refraction of the O-mode and the cutoff of the X-mode beams. That simulation was achieved with a line average density of  $2.4 \times 10^{-19} \text{ m}^{-3}$ . With this value, the maximum density near the center of the plasma reaches  $3.7 \times 10^{-19} \text{ m}^{-3}$ , close to the X-mode cutoff density at 80 GHz we previously found. The cut-off limit, as expected, is higher for the O-mode and for the higher frequencies. This is an important consideration, which means that during V-ECE experiments, we will certainly hit the limit for beam refraction before the limit of the wave cutoff. To minimize the antenna beam refraction in the plasma, one needs to infer quantitative information from the simulation. For that, we attempt to estimate the density limit for refraction using the simulations. The attempt consists of a few steps. First, we find an optimal number of rays to model the antenna pattern. The set of rays is propagated through the plasma, and the trajectory for each ray is computed and recorded at the height of the viewing dump to quantify the effect of refraction in the plasma. The rays are weighted such that the intensity in the beam forms a Gaussian beam pattern with a  $1/e^2$  power level wide 10 cm in diameter.

The analysis allows us to estimate the fraction of the beam intensity that falls out of the dump as a function of discrete values of the electron density in the plasma. The result shown in Fig. 14 refers

to the X-polarization only, for which the density limit is the most constraining. At high frequencies (e.g., 150 GHz), the antenna beam intensity falls quasi-entirely within the viewing dump until we reach a line averaged density of  $2.4 \times 10^{-19} \text{ m}^{-3}$ , corresponding to a maximum density in the plasma of  $3.7 \times 10^{-19} \text{ m}^{-3}$ . The density limit at this frequency is practical, allowing operation of the V-ECE diagnostic in most plasma conditions. The situation at low frequencies instead is essentially unpractical. The refraction constrains V-ECE measurements to be achieved in plasmas with line averaged densities  $\sim 0.4 \times 10^{-19} \text{ m}^{-3}$  corresponding to a maximum density in the plasma of  $\sim 0.6 \times 10^{-19} \text{ m}^{-3}$ . At a line density of  $\sim 0.8 \times 10^{-19} \text{ m}^{-3}$  (maximum density  $\sim 1.2 \times 10^{-19} \text{ m}^{-3}$ ), half the beam intensity at 80 GHz would already miss the dump. This sets the maximum density for refraction to a stringent value below  $1 \times 10^{-19} \text{ m}^{-3}$ . This strong electron density constraint on the window of operation of the V-ECE motivates the search for refraction mitigation techniques.

The first attempts consisted of working at low density or modifying plasma parameters such as the plasma height in the vessel, plasma triangularity, and elongation. Those attempts were not successful on TCV. The effective approach, in order to mitigate the refraction of the antenna beam in the plasma, is related to multiple wall reflections. When the antenna beam pattern is shifted out of the viewing dump, the risk for the diagnostic is the contamination of the non-thermal emission by the background radiation via multiple wall reflections. The measured radiation in that case is a combination, difficult to disassemble, of the background radiation and the non-thermal radiation. The modeling of multiple wall reflections in order to assess their contribution to the detected radiation has been attempted over the years in some ECE studies (see Refs. 19 and 20 for example). The difficulties in using a reflection model to separate the various contributions lie in the complicated geometry of the vessel tiles, the wave diffraction on the tile apertures, and the change in polarization of the wave at each reflection. It was discovered on TCV, an approach that goes around both

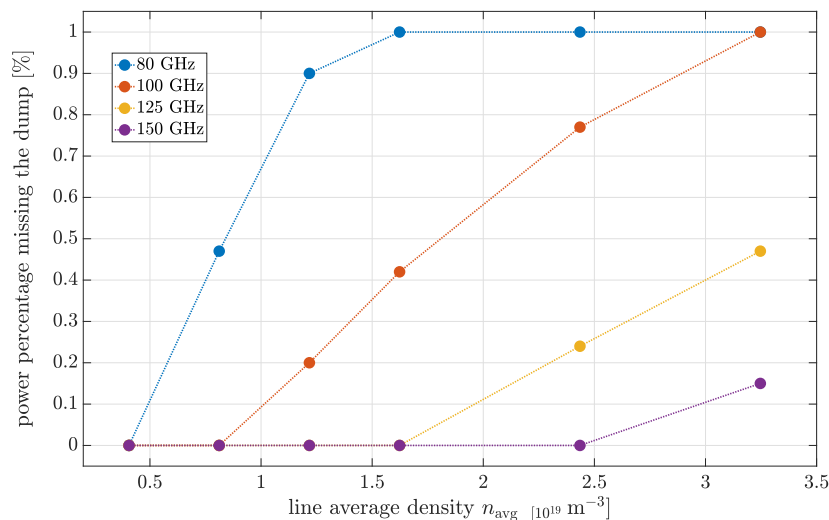


FIG. 14. Density threshold for refraction at different frequencies calculated with the same plasma equilibrium.

the modeling of multiple wall reflections and the operation of the diagnostic at a highly constrained electron density. The approach exploits the fact that the origin of the thermal background can be kept out of the vessel and will thus not pollute the measurement even in conditions of refraction of the antenna pattern out of the viewing dump. In theory, the thermal background can originate exclusively in the discrete radial locations of the cold resonances of the contributing harmonics. The radial location,  $R_{nece}$ , of the cold resonance at a harmonic  $n$  of a given frequency  $f_{nece}$  is a function of the only central magnetic field in the machine,  $B_0$ . An expression of  $R_{nece}$  is given, using the resonance condition in tokamaks, by the equation

$$R_{nece} = \frac{n|e_{ch}|B_0R_0}{2\pi m_{e0}f_{nece}}. \quad (8)$$

From the manipulation of Eq. (8), we can calculate that just two consecutive harmonics can be located together within the vessel and thus contribute to the thermal background on TCV. Considering the magnetic fields and the frequency range, there is no possibility for the cold resonance of the first harmonic to be located within the vessel. The higher harmonics, which are optically thick for the extraordinary polarization, are the ones that can contribute to the background radiation. This means that the thermal background that can be measured by the refracted antenna beam originates on TCV essentially as an X-mode emission from a known location that depends on the magnetic field only. The magnetic field determines, for a given frequency band, the location of the resonances of the thermal X-mode emission. Depending on the field value, the two contributing harmonics within the vessel can be X2 and X3 or X3 and X4 for example. It can be shown that the X2 emission, which reaches the black-body level, dominates over the X3 emission ( $X2/X3 \gg 1$ ). Therefore, the background radiation can be considered on TCV to originate essentially from the X2 emission. That is because the ratio of the black-body intensity (X2) to the X3 intensity is a function of the plasma optical depth. In a plasma with an

electron temperature,  $T_e \sim 1$  keV, and density,  $n_e \sim 1 \times 10^{19} \text{ m}^{-3}$ , the ratio  $X2/X3$  reaches values close to  $\sim 20$ . Since both the X2 and X3 emissions undergo wall reflections in the same conditions and the scrambling on the tiles does not depend on the harmonic number, we deduce that the ratio of the multiply reflected radiation ( $X2_{\text{refl}}/X3_{\text{refl}}$ ) is of the same order as the ratio  $X2/X3$  of the single pass intensities. We note that the X3 optical depth scales like  $n_e T_e^2$ , so the ratio  $X2/X3$  decreases with increasing electron temperature. Calculations at temperatures of  $\sim 4$  keV yield a ratio  $X2/X3$  still high enough to neglect the X3 contribution to the background radiation on TCV. Moreover, neglecting the X3 contribution is necessary, which means neglecting the higher harmonic contribution. Based on these findings, it appeared that a way to avoid multiple wall reflections is to simply keep the X2 cold resonance radius out of the machine. This allows us to relax the constraint on the electron density.

### C. Harmonic overlap

It has been shown, using the V-ECE resonance, the possibility of directly determining the electron energy from the radiation frequency of the electron cyclotron emission. The proviso is to have the emission originating come from a fixed harmonic. From Eq. (3), we note that the higher the harmonic number, the higher the electron energy emitting at a fixed frequency. We calculate the maximum energy to avoid harmonic overlap between the harmonics  $n$  and  $n+1$ , as

$$E_{\text{max}} = \frac{m_{e0}c^2}{n} \sim \frac{511 \text{ keV}}{n}. \quad (9)$$

Equation (9) shows how severe the harmonic overlap is at higher harmonics compared to the lower ones. That is due to the decreasing ratio of consecutive harmonic frequencies to increasing harmonic numbers. The maximum energy that can be measured without harmonic overlap and the ratio of harmonic frequencies,  $f_{(n+1)\text{ece}}/f_{nece}$ ,

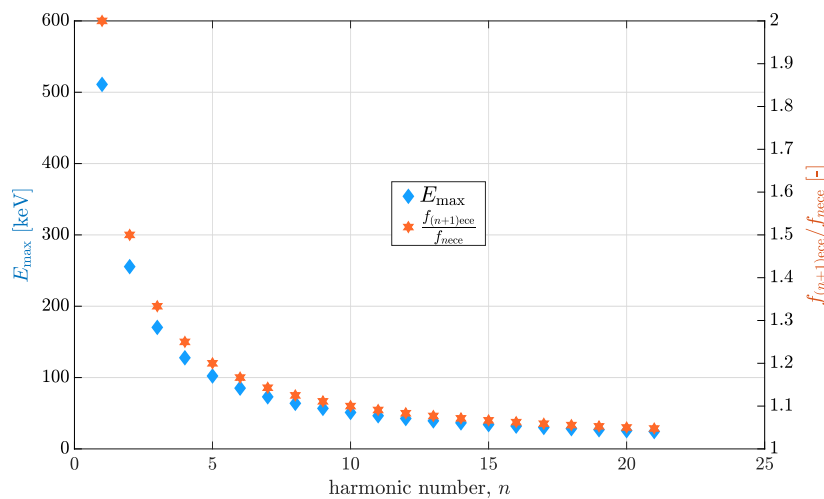


FIG. 15. Maximum energy to avoid harmonic overlap ( $E_{\text{max}}$ ), shown together with the ratio of the harmonic frequencies  $f_{(n+1)\text{ece}}/f_{nece}$ .

are plotted in Fig. 15. Measurements below the fundamental frequency push the energy boundary for harmonic overlap above  $\sim 511$  keV. This energy boundary is already below  $\sim 100$  keV from the fifth harmonic.

#### IV. CALIBRATION

##### A. Idea and results

The results obtained in the assessment of the conditions for V-ECE measurement foster a calibration approach that uses the plasma itself. The technique is based on the calculation of the X3 radiation intensity under conditions of low optical thickness and is validated against the plasma black-body emission, which depends solely on the electron temperature. While the technique is described elsewhere,<sup>16</sup> we present in this section the basic idea and the obtained results. Figure 16 shows the measurement from the V-ECE in a thermal discharge with two magnetic field ramps. As expected, the reflected X3 thermal radiation is dwarfed by the instrumental noise in between the thermal, single pass, X3 emissions. A synthetic ECE, which is used to predict the single pass radiation during the discharge, provides the X3 radiation intensity, which is sufficient for the calibration of the full discharge. The radiation power deduced at the high field, when the plasma radiates as a black body, is used for the validation of the calibration approach. The results of this calibration technique on the V-ECE of TCV suggest a good relative calibration and an absolute calibration with an uncertainty of up to 25%.

#### V. MEASUREMENTS

The measurements shown in this section are examples of V-ECE measurements achieved on TCV. During these measurements, the non-thermal electrons are created by Electron Cyclotron Heating, ECH. The selected measurements show X-polarized radiation from the plasma. The signals are chosen in the frequency range 96–114 GHz for a better quality of the data compared to the lower frequencies, as discussed in Sec. III B.

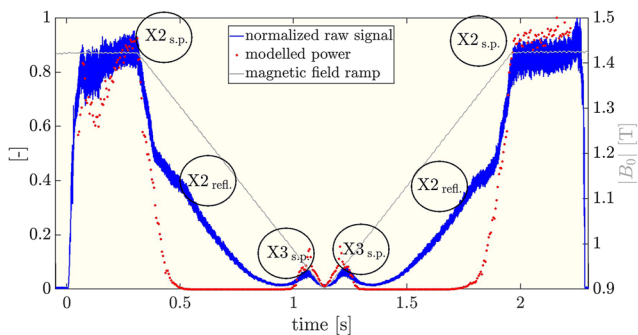


**FIG. 16.** Measurement and modeling used for the calibration of the V-ECE diagnostic. The measurement during magnetic field ramps shows detected X2 and X3 single pass radiation (X2, X3 s.p.) and multiple wall reflected X2 radiation (X2 refl.). The modeling well captures the trend of the single pass radiation and is used to calibrate the measured data.

##### A. Current drive and calibration combined

The plasma discharge #73217 shown in Fig. 17 is designed to combine the calibration of the radiometer and the measurement during current drive. The heating phase for the current drive is achieved in the discharge at a constant magnetic field of  $\sim 1.54$  T for about 1 s between 0.3 and 1.3 s. When the heating is turned off, the value of magnetic field strength is kept unchanged for about 100 ms, until about 1.4 s. The field is then ramped down from 1.54 to 0.9 T in the remaining part of the discharge. The heating phase occurs at a constant ECH power of  $\sim 500$  kW and a constant launcher angle,  $\theta_l \sim 10^\circ$ , at a frequency of  $\sim 82$  GHz. The launcher angle is used to control the direction of the ECH wave vector with respect to the toroidal magnetic field in the plasma. When that angle is close to 0, the ECH wave purely heats the plasma by increasing the perpendicular energy of the bulk electrons. Increasing the launcher angle allows the resonance of the ECH wave with higher energy electrons. The plasma current is ramped down together with the magnetic field such that the equilibrium remains quasi frozen. That is performed in order to preserve the same X-mode polarization from the current drive to the calibration phase. The measured intensity for X-mode radiation in the frequency range 96–114 GHz is also shown in Fig. 18. From the radiometer response, a clear distinction between the two phases can be made. The smooth ramp of the field allows the identification of the thermal peaks for each frequency. The higher frequencies, measuring the lower energies, have their thermal resonances first, followed by the lower frequencies. The energies attributed to the frequencies are those corresponding to the constant field current drive phase of the discharge.

One of the most interesting features of discharge #73217 can be observed in the time interval between 1.3 and 1.4 s, highlighted in Fig. 17. The time interval of  $\sim 100$  ms corresponds to the period after the current drive and before the field ramp. In the interval, the heating is turned off, and the measured energies are kept equal by preserving the field value. The radiation intensity drops for all the measured energies as soon as the heating is turned off. The reduction in the radiation intensity signifies that the radiation measured during the current drive is essentially that of non-thermal electrons, with little or no thermal contribution, depending on the frequency. For illustration, we consider the relatively high frequency of 112 GHz, measuring electrons at an energy of  $\sim 84$  keV. In general, the detected radiation during the current drive phase is the sum of both non-thermal radiation and thermal radiation from multiple wall reflections. The field value in the time interval between 1.3 and 1.4 s keeps the X2 cold resonance of the frequency 112 GHz out of the plasma, with the consequence of a very low level of radiation measured when the heating is off. Since the X2 cold resonance in that interval is at the same location as it was during the heating phase, we can conclude that the radiation measured during the current drive is essentially that of non-thermal electrons at  $\sim 84$  keV. The clean measurement of non-thermal emission at 112 GHz is possible due to the absence of background radiation, whose origin is kept out of the plasma for that frequency. For the lowest frequencies, measuring the higher energies, the observation is consistent. The intensity that is measured at the highest energies during the transition phase can be attributed to the background radiation. The intensity level of the background radiation is higher at lower frequencies. That is

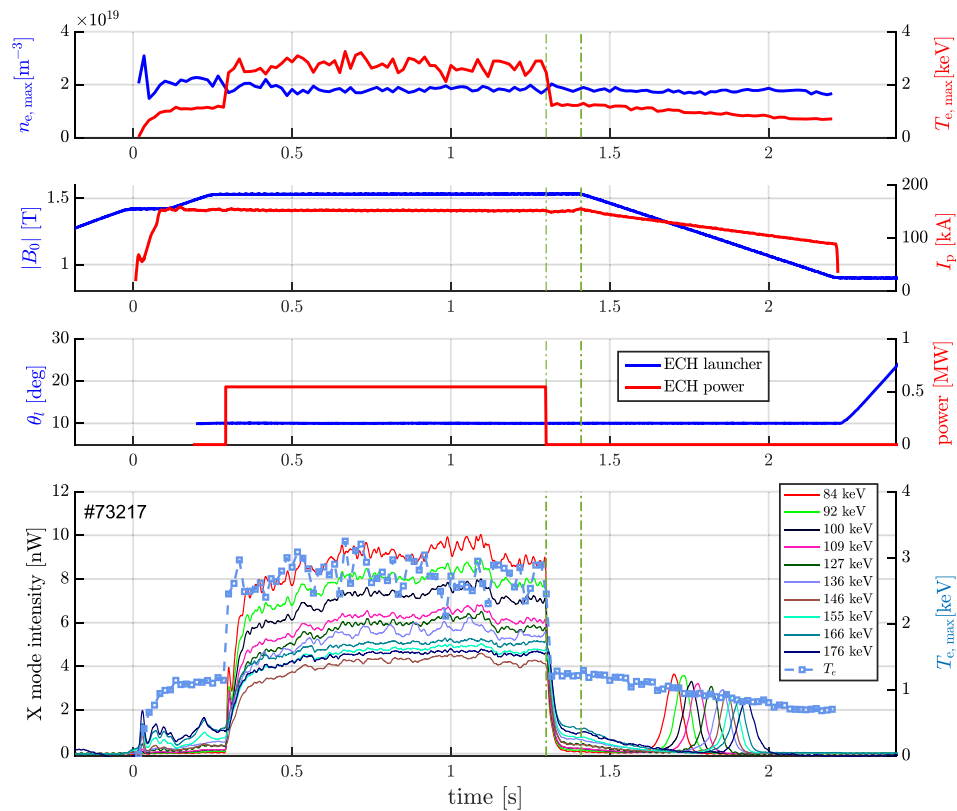


**FIG. 17.** V-ECE measurement with combined calibration and current drive for TCV discharge #73217. The current drive is achieved at constant magnetic field from 0.3 to 1.3 s. The vertical green lines delimit the period of time in which the field is kept constant and the ECH power is turned off. The field is ramped down starting at 1.4 s for the calibration phase.

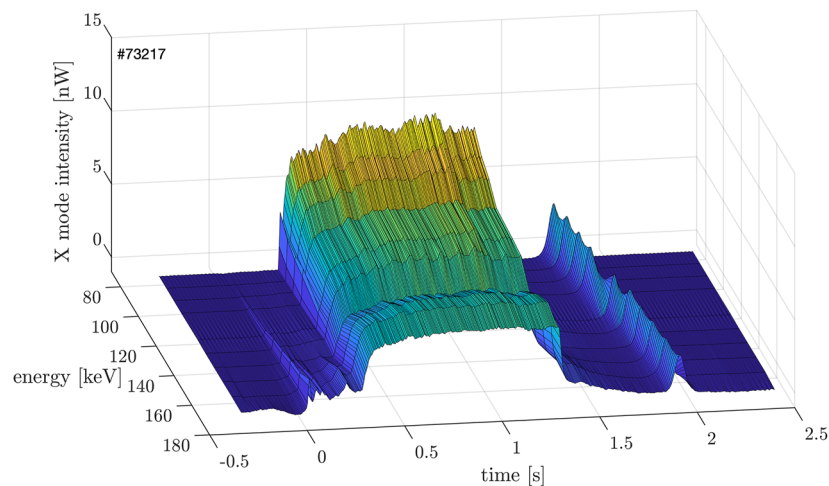


**FIG. 18.** Three dimensional plot of the measurement during the hybrid TCV discharge #73217 combining calibration and current drive.

because the X2 cold resonances of the lower frequencies are located at smaller major radii in the plasma. For some of the frequencies, those having their thermal X2 in the plasma, the measured radiation during current drive is a combination of both thermal and non-thermal radiation at the calculated energies. These observations consolidate the findings on the conditions for non-thermal electron measurement with the diagnostic.

The three dimensional plot in Fig. 18 shows the two phases of the discharge with the transition interval marked by a reduction of the measured intensity in the direction of the lower energies. The thermal peak intensities on which the channels have been calibrated have lower intensities with increasing energies (decreasing frequencies). That is due to the drop in electron temperature with the field and current being ramp down. We note an additional feature regarding this discharge, on the relative intensities measured during the current drive phase. During that phase, the launcher angle,  $\theta_l$ , constrains the region in the velocity space that resonates with the ECH wave. For this discharge, the launcher angle was low enough to excite the lower energy electrons. That explains the higher intensity observed at the lower energies. At higher energies, the non-thermal contribution to the radiation adds up to the background radiation explaining the relatively high level of the measured intensity.

There is a region observed in the energy space near  $\sim 150$  keV that exhibits a feature similar to a “valley” in the measured intensity. That region is the transition between two regions of interest. Those regions of interest are (1) the region where the thermal background has a significant contribution to the measured intensity and (2) the region where it is a negligible fraction of the measured intensity. In Fig. 18, the thermal background radiation can be observed over time, before and after the current drive, and also in the energy space, with a decreasing intensity level toward the lowest energies.

## B. Current drive experiment with launcher angle sweep

We present in this section an example of V-ECE measurement during a dedicated Electron Cyclotron Current Drive (ECCD) discharge on TCV. For this discharge, the calibration of the diagnostic is achieved a priori using a different plasma discharge. The ECH power had a value similar to that of the hybrid discharge #73217, while the launcher angle was varied in five stationary steps during the heating phase between 0.7 and 1.9 s. Here as well, the toroidal angle of the X2 launcher was kept constant at  $\sim -90^\circ$ . The variation of the poloidal angle of the launcher from  $\sim 10^\circ$  to  $\sim 26^\circ$  in

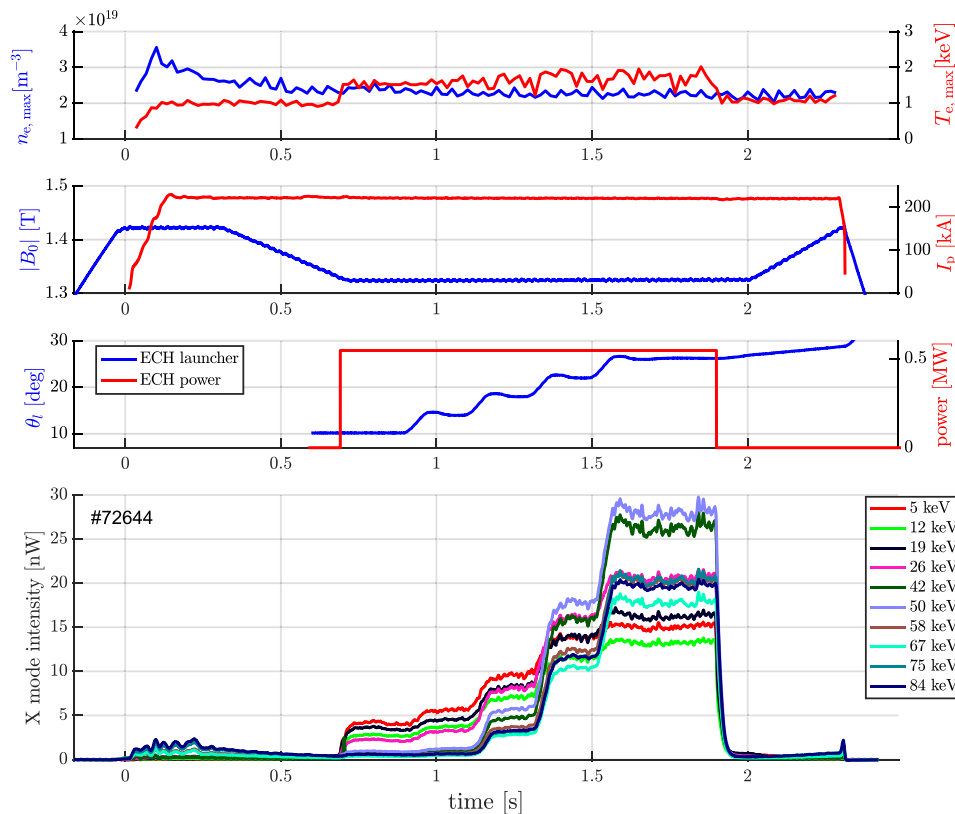


**FIG. 19.** V-ECE measurement during a current drive experiment with swept launcher angle during TCV discharge #72644. The current drive is achieved at constant magnetic field and constant ECH power.

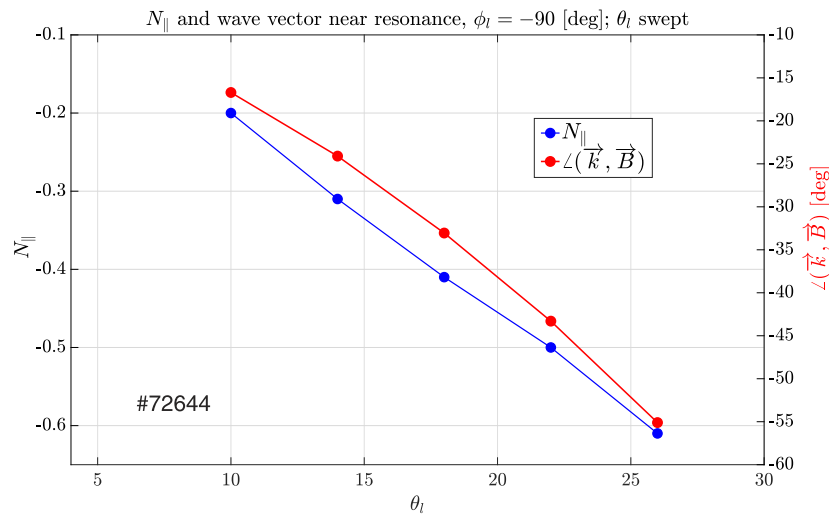


FIG. 20. Parallel refractive index and ECH wave angle as a function of the launcher poloidal angle, during the TCV plasma discharge #72644.

each stationary step allows the observation of stair-shape X-mode intensities (see Fig. 19). An assessment of the measured energy allows us to analyze the discharge following the dynamics in the phase space. When the heating is turned on during the discharge #72644, at  $\sim 0.7$  s, only the low energies ( $\sim 5$  to 26 keV) exhibit a sharp jump in the measured intensity. The intensity at the higher energies ( $\sim 67$  to 75 keV) experiences a similar jump, with a delay of more than  $\sim 500$  ms, when the launcher angle has been moved to its third stage. From that moment on, the dynamics is inverted, and the higher energies now experience the sharpest jump in intensity compared to the lower energies. Interestingly, the measurement at the middle energies in our range will then reach the highest value of intensity when the launcher angle reaches its last stage.

The parallel refractive indices of the ECH wave, computed at the location of maximum absorption, are shown in Fig. 20. As expected, the increase in the launcher poloidal angle allows us to achieve higher values (in absolute terms) of the parallel refractive index at the wave absorption location. The physical mechanisms of the plasma-wave interaction are complex. The mechanisms include in general, momentum diffusion and pitch-angle scattering, which make the ECCD resonant interaction region complex to determine. What can be said for the interpretation of this experiment is that higher values  $\theta_l$  and thus  $N_{\parallel}$  induce more energetic electrons in the plasma, explaining the different jumps in the measured intensities.

## VI. CONCLUSION AND OUTLOOK

A Vertical ECE (V-ECE) diagnostic has been built and commissioned on the TCV tokamak. The diagnostic exploits a heterodyne receiver for highly resolved measurements of the X- and O-mode polarized radiation during non-thermal electron experiments. The energy resolution of the diagnostic system is primarily influenced by the antenna beam size. The observation of an operational window

where the thermal background radiation does not pollute the measurement allows the calibration of the diagnostic using plasma measurements and modeling. Future work with the diagnostic includes the measurement of the electron energy distribution during runaway electron experiments and current drive experiments on TCV, with comparison with Fokker-Planck modeling.

## ACKNOWLEDGMENTS

The authors acknowledge the fruitful discussion with Lorenzo Figini and acknowledge the CNR-ISTP for providing the SPECE software used for the antenna modeling. This work has been carried out within the framework of the EUROfusion Consortium via the Euratom Research and Training Program (Grant Agreement No. 101052200—EUROfusion) and funded by the Swiss State Secretariat for Education, Research and Innovation (Staatssekretariat für Bildung, Forschung und Innovation—SBFI). The views and opinions expressed are, however, those of the author(s) only and do not necessarily reflect those of the European Union, the European Commission, or SBFI. Neither the European Union nor the European Commission nor SBFI can be held responsible for them. This work was supported in part by the Swiss National Science Foundation.

## AUTHOR DECLARATIONS

### Conflict of Interest

The authors have no conflicts to disclose.

## Author Contributions

**A. Tema Biwole:** Conceptualization (equal); Data curation (equal); Formal analysis (equal); Investigation (equal); Methodology (equal); Writing – original draft (equal); Writing – review & editing (equal). **L. Porte:** Conceptualization (equal); Funding acquisition



(equal); Investigation (equal); Methodology (equal); Supervision (equal); Validation (equal); Writing – review & editing (equal). **S. Coda:** Conceptualization (equal); Methodology (equal); Supervision (equal); Writing – review & editing (equal). **A. Fasoli:** Conceptualization (equal); Funding acquisition (equal); Supervision (equal); Writing – review & editing (equal).

## DATA AVAILABILITY

The data that support the findings of this study are available from the corresponding author upon reasonable request.

## REFERENCES

- <sup>1</sup>M. Bornatici, R. Cano, O. De Barbieri, and F. Engelmann, “Electron cyclotron emission and absorption in fusion plasmas,” *Nucl. Fusion* **23**(9), 1153–1257 (1983).
- <sup>2</sup>I. H. Hutchinson, *Principles of Plasma Diagnostics* (Cambridge University Press, 2002).
- <sup>3</sup>H. J. Hartfuss and T. Geist, “Chapter 4: Passive diagnostics,” in *Fusion Plasma Diagnostics with mm-Waves* (John Wiley and Sons, Ltd, 2013), pp. 117–150.
- <sup>4</sup>P. Blanchard, S. Alberti, S. Coda, H. Weisen, P. Nikkola, and I. Klimanov, “High field side measurements of non-thermal electron cyclotron emission on TCV plasmas with ECH and ECCD,” *Plasma Phys. Controlled Fusion* **44**, 2231 (2002).
- <sup>5</sup>I. Klimanov, “Reconstruction of the electron distribution function during ECRH/ECCD and magnetic reconnection events in a tokamak plasma,” Ph.D. thesis, Ecole Polytechnique Fédérale de Lausanne, 2005.
- <sup>6</sup>I. H. Hutchinson, K. Kato, and S. C. Texter, “Measurements of mildly relativistic electron distribution functions during lower hybrid heating and current drive (invited),” *Rev. Sci. Instrum.* **57**, 1951 (1986).
- <sup>7</sup>T. C. Luce, P. C. Efthimion, and N. J. Fisch, “Superthermal electron distribution measurements from polarized electron cyclotron emission (invited),” *Rev. Sci. Instrum.* **59**, 1593 (1988).
- <sup>8</sup>G. Giruzzi, J.-L. Ségui, A.-L. Pecquet, and C. Gil, “Observation of the  $m = 1$  mode by microwave transmission measurements in TORE SUPRA,” *Nucl. Fusion* **31**, 2158–2162 (1991).
- <sup>9</sup>G. Giruzzi, J. L. Ségui, T. D. de Wit, Y. Michelot, Y. Peysson, D. Moreau, and M. Talvard, “Measurement of the time constants of fast electron distributions in the Tore Supra tokamak,” *Phys. Rev. Lett.* **74**, 550–553 (1995).
- <sup>10</sup>D. R. Roberts, R. F. Steimle, G. Giruzzi, G. Cima, and C. Watts, “Vertical viewing of electron-cyclotron emissions for diagnosing fast-electron dynamics in TEXT-U,” *Rev. Sci. Instrum.* **66**, 427–429 (1995).
- <sup>11</sup>R. James, S. Janz, R. Ellis, D. Boyd, and J. Lohr, “Vertical-viewing electron cyclotron emission diagnostic for the DIII-D tokamak,” *Rev. Sci. Instrum.* **59**, 1611 (1988).
- <sup>12</sup>M. Farnik, J. Urban, J. Zajac, O. Bogar, M. Varavin, A. Casolari, J. Cerovsky, O. Ficker, J. Mlynar, E. Macusova, V. Weinzettl, and M. Hron, “Radiometry for the vertical electron cyclotron emission from the runaway electrons at the COMPASS tokamak,” *Rev. Sci. Instrum.* **90**, 113501 (2019).
- <sup>13</sup>A. Tema Biwole, L. Porte, A. Fasoli, A. Simonetto, and O. D’Arcangelo, “Performance of a high vacuum, high temperature compatible millimeter-range viewing dump for the vertical ECE experiment on TCV,” *Fusion Eng. Des.* **162**, 112079 (2021).
- <sup>14</sup>D. Farina, L. Figini, P. Platania, and C. Sozzi, “SPECE: A code for electron cyclotron emission in tokamaks,” *AIP Conf. Proc.* **988**, 128 (2008).
- <sup>15</sup>P. F. Goldsmith and E. L. Moore, “Gaussian optics lens antennas,” *Microwave J.* **27**, 153 (1984).
- <sup>16</sup>A. Tema Biwole, “Measuring the electron energy distribution in tokamak plasmas from polarized electron cyclotron radiation,” Ph.D. thesis, Ecole Polytechnique Fédérale de Lausanne, 2023.
- <sup>17</sup>F. Felici, “ECPOL: Equations and MATLAB tools for EC wave reflection and polarization calculations,” Technical Report No. LRP 01/2012, Centre des Recherches en Physique des Plasmas, Ecole Polytechnique Fédérale de Lausanne, 2012.
- <sup>18</sup>L. Figini, “Electron cyclotron emission in tokamaks: Development of a new modeling tool for data validation, analysis and predictions,” Ph.D. thesis, Università degli Studi di Milano, 2009.
- <sup>19</sup>A. E. Costley, R. J. Hastie, J. W. M. Paul, and J. Chamberlain, “Electron cyclotron emission from a tokamak plasma: Experiment and theory,” *Phys. Rev. Lett.* **33**, 758–761 (1974).
- <sup>20</sup>L. Figini, “Electron cyclotron emission in tokamaks: Development of a new modelling tool for data validation, analysis and predictions,” Ph.D. thesis, Università degli studi di Milano, 2009.